

Journal of Biomedical Optics

BiomedicalOptics.SPIEDigitalLibrary.org

Static laser speckle contrast analysis for noninvasive burn diagnosis using a camera-phone imager

Sigal Ragol
Itay Remer
Yaron Shoham
Sivan Hazan
Udi Willenz
Igor Sinelnikov
Vladimir Dronov
Lior Rosenberg
Alberto Bilenca

Static laser speckle contrast analysis for noninvasive burn diagnosis using a camera-phone imager

Sigal Ragol,^a Itay Remer,^a Yaron Shoham,^b Sivan Hazan,^a Udi Willenz,^c Igor Sinelnikov,^d Vladimir Dronov,^d Lior Rosenberg,^b and Alberto Bilenca^{a,e,*}

^aBen-Gurion University of the Negev, Biomedical Engineering Department, 1 Ben Gurion Blvd, POB 653, Beer-Sheva 8410501, Israel

^bSoroka University Medical Center, Ben Gurion University of the Negev, Faculty of Health Sciences, Department of Plastic and Reconstructive Surgery, Rager Blvd, POB 151, Beer Sheva 8410101, Israel

^cLahav CRO Research Unit, POB Negev, Kibbutz Lahav, 8533500, Israel

^dSoroka University Medical Center, Institute of Pathology, POB 151, Beer-Sheva 8410101, Israel

^eBen-Gurion University of the Negev, Ilse Katz Institute for Nanoscale Science and Technology, 1 Ben Gurion Boulevard, P.O. Box 653, Beer-Sheva 8410501, Israel

Abstract. Laser speckle contrast analysis (LASCA) is an established optical technique for accurate widefield visualization of relative blood perfusion when no or minimal scattering from static tissue elements is present, as demonstrated, for example, in LASCA imaging of the exposed cortex. However, when LASCA is applied to diagnosis of burn wounds, light is backscattered from both moving blood and static burn scatterers, and thus the spatial speckle contrast includes both perfusion and nonperfusion components and cannot be straightforwardly associated to blood flow. We extract from speckle contrast images of burn wounds the nonperfusion (static) component and discover that it conveys useful information on the ratio of static-to-dynamic scattering composition of the wound, enabling identification of burns of different depth in a porcine model *in vivo* within the first 48 h postburn. Our findings suggest that relative changes in the static-to-dynamic scattering composition of burns can dominate relative changes in blood flow for burns of different severity. Unlike conventional LASCA systems that employ scientific or industrial-grade cameras, our LASCA system is realized here using a camera phone, showing the potential to enable LASCA-based burn diagnosis with a simple imager. © The Authors. Published by SPIE under a Creative Commons Attribution 3.0 Unported License. Distribution or reproduction of this work in whole or in part requires full attribution of the original publication, including its DOI. [DOI: [10.1117/1.JBO.20.8.086009](https://doi.org/10.1117/1.JBO.20.8.086009)]

Keywords: medical optics; medical instrumentation; speckle; imaging.

Paper 150038RR received Jan. 23, 2015; accepted for publication Jul. 6, 2015; published online Aug. 13, 2015.

1 Introduction

Laser speckle contrast analysis (LASCA) is a relatively simple imaging method that utilizes spatial statistics of time-integrated speckle to obtain two-dimensional spatial maps of relative blood flow speed over a wide field-of-view with no scanning. In LASCA, the speckle contrast, defined as the ratio of the spatial standard deviation to the mean speckle intensity, is measured to quantify the degree of local blurring in the speckle image, which is directly related to tissue blood perfusion when no or minimal scattering from static tissue elements is present.¹ As a result, LASCA has been proven effective in estimating relative blood flow in the retina²⁻⁴ and exposed brain⁵⁻⁷ and skin⁸ microcirculation. However, LASCA imaging in the presence of static scattering (from the skull or burn layer of skin, for instance) yields a spatial speckle contrast that includes contributions from both dynamic and static scatterers in the sample. This requires the use of novel methods that can improve estimation of the dynamic (perfusion) and static (nonperfusion) speckle components from the measured speckle contrast; otherwise, interpretation of the speckle contrast as an accurate estimate of relative blood flow speed can be confounding.^{1,9-13}

Over the past several years, a few laser speckle-based imaging techniques have been devised to enable access to perfusion

and nonperfusion information inherent in the spatial laser speckle contrast recorded for samples that contain both dynamic and static scatterers. One such method is dynamic laser speckle imaging (LSI) that evaluates the fraction of statically scattered light from the total detected intensity using a standard LASCA imaging system and a novel processing scheme in order to improve estimation of the perfusion rate from the measured spatial speckle contrast.⁹ Dynamic LSI was used for *in vivo* hemodynamic brain imaging through thinned and intact skulls of rodents and showed improved assessment of relative cerebral perfusion levels.¹⁰ Another technique is multiexposure speckle imaging that fits multiple-exposure spatial speckle contrast data to a novel speckle model that includes both perfusion and nonperfusion components to provide accurate flow measurements in the presence of static scattering.¹¹ Multiexposure speckle imaging was employed to more accurately evaluate *in vivo* blood flow changes in mice brain through thinned skull¹² and skin perfusion.¹³

In this work, we use the processing scheme of dynamic LSI to improve estimation of the dynamic (perfusion) and static (nonperfusion) speckle contrast components from the speckle contrast measured by LASCA in burn phantoms and in a porcine burn model. In contrast to typical LASCA imaging systems that utilize scientific or industrial-grade cameras, we realize here a LASCA imaging instrument with a simple camera-phone imager.¹⁴ Importantly, recent LASCA imaging systems using

*Address all correspondence to: Alberto Bilenca, E-mail: bilenca@bgu.ac.il

simple imagers, including consumer-grade color cameras, webcams, and camera phones, have been shown to be useful for blood perfusion imaging of the human palm and mouse brain.^{15–17} From the perfusion and nonperfusion speckle contrast components, we extract the reciprocal of the speckle correlation time, τ_c^{-1} , and the statically-to-dynamically scattered light ratio (SDR), which provide corrected estimates for blood perfusion and static-to-dynamic scattering composition ratio of burn wounds, respectively. We then show that the SDR, rather than τ_c^{-1} , can largely control the ability of the speckle contrast to distinguish burns of different severity with statistical significance. Hence, we termed the processing scheme static laser speckle contrast analysis (stLASCA).

The paper is organized as follows. Section 2 describes the camera-phone LASCA imaging instrument and outlines methods for stLASCA processing, preparation of the burn phantoms, and use of the porcine burn model including histopathology and statistical analysis of porcine burn depth. In Sec. 3, we present results and discussion of stLASCA in flow and burn phantoms and in a porcine model *in vivo* over 104 hours postburn (hpb). Finally, conclusions are drawn in Sec. 4.

2 Methods and Materials

2.1 Camera-Phone Laser Speckle Contrast Analysis Imaging Instrument

The camera-phone LASCA imaging system employed in this work is shown in Fig. 1(a). A linearly polarized red He–Ne laser beam (CVI Melles-Griot), reshaped by an engineered diffuser (Thorlabs) to a ~ 5 -cm diameter circle beam, illuminated the sample with an intensity of 0.2 mW/cm^2 , well below the maximum permissible exposure of skin at 633 nm, as indicated by the American National Standards Institute.¹⁸ Backscattered light from the sample was then projected onto a back-illuminated CMOS sensor of an eight megapixel camera phone with a bit depth of 8 bits per color channel (Sony-Ericsson)¹⁹ through a polarizer with its polarization axis perpendicular to the illumination polarization and a $10\times$ zoom lens (Computar).¹⁴ The crossed polarizers rejected specular reflections from the sample surface, and the zoom lens was set to a magnification of 0.07 and an f -stop of 8, yielding ~ 12 to 16 pixels/speckle with ~ 3 to 4 red Bayer pixels and ~ 9 to 12 red interpolated pixels. Note that for our application of LASCA with a red He–Ne laser and

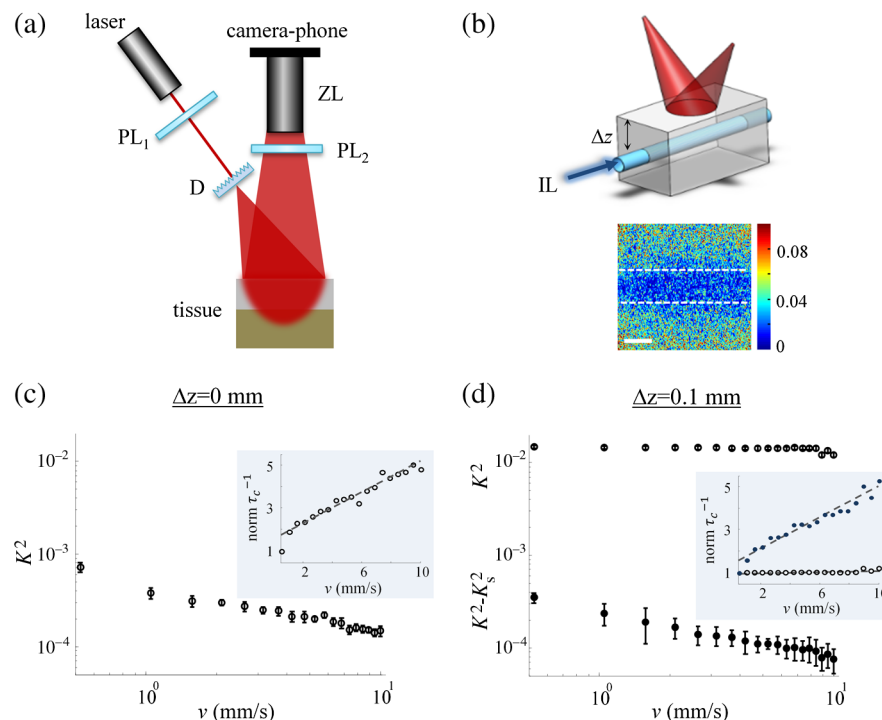


Fig. 1 Camera-phone laser speckle contrast analysis imaging. (a) Experimental arrangement. $PL_{1/2}$, crossed polarizers; D, engineered diffuser; ZL, $10\times$ zoom lens. (b) Top panel: schematics of the flow/burn phantom used in this work. The phantom consisted of Intralipid (IL) flowing in a polycarbonate tube at speed v . The tube was embedded within a statically scattering Teflon slab at various depths, Δz , or, alternatively, was exposed to air (that is, $\Delta z = 0 \text{ mm}$) to obtain phantoms with insignificant static scattering. Bottom panel: representative K^2 -map of a flow phantom with $v = 10 \text{ mm/s}$ and $\Delta z = 0.1 \text{ mm}$. The perfused region is outlined with dashed lines. High and low K^2 values are indicated in red and blue colors, respectively. The solid bar corresponds to 1 mm . (c) K^2 versus v in a double-logarithmic scale obtained from flow phantoms with insignificant static scattering. The mean (circles) and standard deviation (error bars) of K^2 calculated over 30 successive speckle frames are shown. The inset presents normalized τ_c^{-1} against v . (d) K^2 (open circles) and $K^2 - K_s^2$ (solid circles) versus v in a double-logarithmic scale obtained from flow phantoms with larger static scattering ($\Delta z = 0.1 \text{ mm}$). The mean (circles) and standard deviation (error bars) of K^2 and $K^2 - K_s^2$ calculated over 30 successive speckle frames are shown. The inset displays normalized τ_c^{-1} against v without (open circles) and with (solid circles) correction for static scattering. Normalization of τ_c^{-1} was performed with respect to τ_c^{-1} at the lowest flow speed ($v = 0.5 \text{ mm/s}$).

throughout all experiments, we only utilized the red channel of the demosaiced (interpolated) Bayer data provided by the camera-phone sensor. Finally, the instrument was mounted on a support arm that allowed appropriate orientation placement and stabilization of the system over the sample, thereby eliminating undesired motion of the instrument during data acquisition.

2.2 Laser Speckle Contrast Analysis and Static Laser Speckle Contrast Analysis

Videos of speckle patterns were captured with 720p resolution at 30 frames/s by the camera-phone imager. The videos were compressed using H.264, which is a lossy video compression technique that attempts to eliminate duplicate image data between frames (e.g., background information) while estimating image motion data from neighboring frames.²⁰ The acquired sequence of speckle images was subsequently processed using MATLAB (Mathworks) on a standard personal computer to quantify the spatial laser speckle contrast and its nonperfusion and perfusion components, from which we recovered the SDR and the reciprocal of the speckle correlation time, τ_c^{-1} , of the scattering medium, respectively.

The spatial laser speckle contrast, K , is given by¹

$$K = \frac{\sigma}{\mu}, \quad (1)$$

where μ and σ denote the local mean and standard deviation of the speckle intensity pattern, respectively. In LASCA, the estimations for μ and σ (and hence K) were computed as the sample mean and the square root of the sample variance of the speckle image, respectively, over spatial windows of 200×1000 pixels (for the flow and burn phantoms) and 200×200 pixels (for the porcine burns). To reduce measurement noise, the final spatial speckle contrast was obtained by averaging 15 to 30 K^2 values evaluated over successive speckle frames. To produce K^2 -maps, a sliding window of 5×5 pixels was applied to 15 to 30 consecutive speckle frames, which were then averaged for noise reduction. Importantly, in the *in vivo* porcine model study, 15 speckle contrast values were acquired over 0.5 s during exhalation intervals of ~ 1.25 s. The data exhibited a steady level of contrast in these time intervals and were further averaged for noise reduction, thus minimizing breathing artifacts.

The static (nonperfusion) speckle contrast component, K_s , of the spatial laser speckle contrast, K , reads as (see Appendix)^{9,10}

$$K_s = \beta^{1/2} \rho, \quad \rho = \frac{I_s}{I_s + I_d}, \quad (2)$$

where ρ is the fraction of total light that is statically scattered, I_s and I_d are the mean intensities of light scattered from the static and dynamic scatterers in the imaged medium, respectively, and β is a normalization coefficient (so-called coherence factor) calibrated here to a value of 0.05 using a Teflon slab with $\rho = 1$.^{9,10} The SDR of the medium can directly be derived from Eq. (2) to be

$$\text{SDR} = \frac{I_s}{I_d} = \frac{\rho}{1 - \rho} = \frac{K_s / \beta^{1/2}}{1 - K_s / \beta^{1/2}}. \quad (3)$$

To retrieve the SDR from the speckle data, Eq. (3) was employed with the estimator for K_s computed by cross-correlating two time-sequential speckle frames across observation

windows of 200×1000 pixels (for the flow and burn phantoms) and 200×200 pixels (for the porcine burns) at zero spatial shift (see Appendix). The estimation of K_s was further improved by averaging multiple K_s values calculated over 15 to 30 time-successive frames.

The dynamic (perfusion) part, K_d , of the speckle contrast, K , is given by (see Appendix)^{9,10}

$$K_d = \left[(1 - \rho)^2 \frac{2\beta}{T} \int_0^T \left(1 - \frac{\tau}{T}\right) |g_d(\tau)|^2 d\tau + 2\rho(1 - \rho) \frac{2\beta}{T} \int_0^T \left(1 - \frac{\tau}{T}\right) |g_d(\tau)| d\tau \right]^{1/2}, \quad (4)$$

where T is the camera integration time. Here, the electric field autocorrelation function $g_d(\tau)$ represents the temporal fluctuations of the speckle field (due to backscattering off moving scatterers in the medium) with characteristic decay time of τ_c . Assuming $T \gg \tau_c$ and a medium with backscattering ballistic or diffusive dynamics and strong multiple scattering, τ_c^{-1} , in the medium can be expressed as (see Appendix)

$$\tau_c^{-1} = \frac{1}{T} \frac{(\beta^{1/2} - K_s)^2 + 4K_s(\beta^{1/2} - K_s)}{K^2 - K_s^2}, \quad (5)$$

where β and K_s were defined in Eq. (2). To recover τ_c^{-1} from the speckle data, Eq. (5) was used with the estimates of K and K_s described above. Because τ_c^{-1} is generally assumed to be proportional to the speed of the moving scatterers in the medium,^{1,21} Eq. (5) provides corrected recovery of flow speed from K^2 in the presence of static scatterers. Note that Eq. (5) converges (up to a proportional constant) to simplified LASCA equations with no or minimal static scattering (that is, $K_s \cong 0$) reported by Cheng and Duong,³ Cheng et al.,⁴ and Ramirez-San-Juan et al.²²

2.3 Flow and Burn Phantoms

Flow phantoms with and without significant static scattering were produced by flowing Intralipid solution (Simga; 9% in absolute concentration) in a 0.6-mm diameter polycarbonate tube (Paradigm Optics) embedded $\Delta z = 0.1$ mm in a statically scattering Teflon slab or exposed to air, respectively, as shown in the upper panel of Fig. 1(b). A range of flow speeds from 0.5 to 10 mm/s was generated using a digital syringe pump (New Era Pump Systems).

To mimic skin burn wounds of different depth and blood flow conditions, we fabricated phantoms comprising a statically scattering Teflon slab within which a 9% Intralipid solution was flowing at 3 and 10 mm/s through a 0.6-mm diameter polycarbonate tube embedded at a depth of $\Delta z = 0.1$ to 1.7 mm below the Teflon–air interface, as illustrated in the upper panel of Fig. 1(b). The Teflon slab, having a reduced scattering coefficient of ~ 35 cm, emulated the upper static burn layer, whereas the 9% Intralipid solution with a reduced scattering coefficient of ~ 25 cm⁻¹ simulated blood in the viable tissue underlying the burn layer.²³ The reduced scattering coefficients of the Teflon and Intralipid solution were measured by oblique-incidence optical reflectometry.²⁴

2.4 Porcine Burn Model

An *in vivo* experiment using a porcine skin burn model was performed at Lahav CRO research unit (Kibbutz Lahav, Israel). The

study protocol was approved by the National Animal Care and Use Committee (#IL-13-05-098) and was executed in accordance with the Guide for the Care and Use of Laboratory Animals. The porcine skin model was selected due to the high resemblance of porcine skin to human skin in terms of structure and wound healing.²⁵ In addition, this model has the advantage of allowing comparison to histopathology which, in most cases, is unavailable in human injuries.

One domestic female pig (*Sus scrofa domestica*), crossbred between Mixed Landrace and Large White, weighing 33 kg and approximately two months old was used in this experiment. The pig was individually housed, had access to water, and acclimated to the facilities for 5 days prior to use. The pig was fasted for 12 h before anesthesia, and hair was removed from the pig dorsum immediately prior to experiment. All burn procedures were performed under general anesthesia, induced by intramuscular injection of Ketamine HCl (Clorketam® 1 g/10 ml, Vetoquinol, Lure, France) 10 mg/kg, Xylazine HCl (Thiazine® 100 mg/ml, Ceva Animal Health Pty LTD, New South Wales, Australia) 2.0 mg/kg, and IV after vein flow insertion of Diazepam (Assival® 10 mg/2 ml, Teva Pharmaceutical Industries Ltd, Hungary) 5 mg/pig. An endotracheal tube was used for mechanical ventilation with 2% to 3% Isoflurane (Ohmeda 7900, Datex-Ohmeda, Inc., Wisconsin). Electrocardiogram, heart rate, O₂ saturation, and body temperature were continuously

monitored throughout the experiment (VitaLogic™ 6000, Men-nen Medical, Pennsylvania).

Forty-eight partial-thickness burns were inflicted by varying the contact time between a brass block heated in boiling water to 100°C and the animal skin.^{25,26} Specifically, twelve 3 × 3 cm² burns were created on the pig dorsum at each of the four contact time of 10, 20, 30, and 40 s, yielding four burn groups. As shown in Fig. 2(a), burns of each group were uniformly distributed across the animal dorsum to reduce the relationship between burn group and position, enabling a longitudinal study with a statistically adequate number of burn biopsies collected from the central field-of-view of the LASCA images. To ensure a contact temperature of 100°C immediately prior to each infliction, the temperature of the brass block was monitored using a thermocouple threaded into the bottom of the block. For each burn site, the brass block was first gently touched to a towel to remove water drops and was subsequently placed on the animal skin. Only the weight of the block was used to form the burns and no additional pressure was applied, as depicted in Fig. 2(b). Furthermore, to avoid variations in creating the burns, one person (Y.S.) created all burns.

2.5 Histopathology

For a blinded histologic analysis, four 4-mm biopsy punches of each burn group (corresponding to contact times of 10, 20, 30, and 40 s) were collected from different locations across the entire animal dorsum at 8, 32, and 104 hpb. Burn regions were punched at the center and were then excluded from subsequent imaging measurements. All biopsies were processed and stained using hematoxylin and eosin (H&E), which darkens in the presence of denatured dermal collagen, yielding histology images, as those shown in Figs. 2(c) and 2(d). To assess burn depth, histological slides were evaluated independently by two pathologists against predetermined histologic criteria,^{27,28} including, for example, disorganization of the basal layer, vascular collapse, eosinophilia (or blurring pattern) of collagen fibers, and empty cavity of the pilosebaceous unit. The burn thickness was determined to be corresponding to the deepest identified histologic feature within the burn under examination. Burn depth was reassessed by both pathologists together in cases where their blind assessment resulted in depth differences larger than 0.1 mm.

2.6 Statistical Analysis

To test the significant difference between the burn groups, a one-way analysis of variance followed by Tukey's *post-hoc* test was performed on histologic burn depth and normalized K^2 , SDR, and τ_c^{-1} measured for four burn groups of contact times of 10, 20, 30, and 40 s at biopsy times of 8, 32, and 104 hpb. K^2 , SDR, and τ_c^{-1} were normalized by the corresponding K^2 , SDR, and τ_c^{-1} values of normal porcine skin measured in a control region on the animal dorsum at the time of biopsy.

3 Results and Discussion

3.1 Validation of the Camera-Phone Laser Speckle Contrast Analysis Imaging Instrument for Perfusion Measurements

To validate the camera-phone LASCA system for perfusion measurements, we studied flow phantoms with and without significant static scattering (see Sec. 2.3). The lower panel of

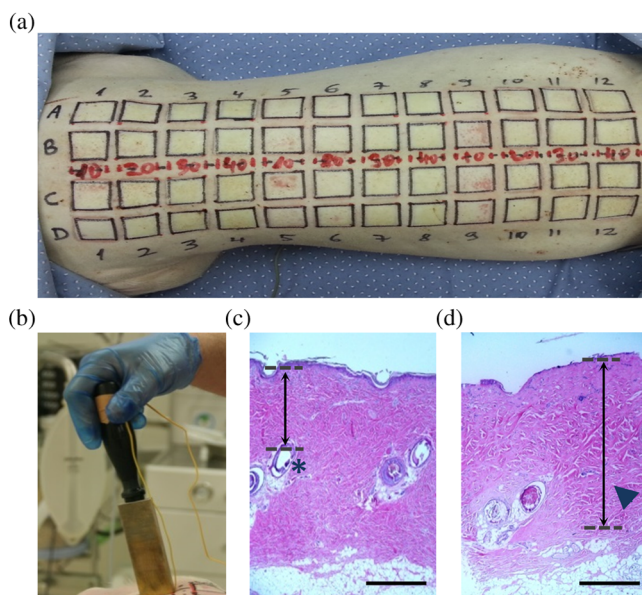


Fig. 2 Porcine skin burn model and histopathology. (a) 48 partial-thickness thermal burns on pig dorsum on either side of the spine are shown at 2 hpb, where the solid lines outline the region of each burn. Contact times between the burn infliction probe and the animal skin are written along the spine of the pig. (b) The infliction probe, made of a brass block, was preheated in boiling water to 100°C. A thermocouple threaded into the bottom of the probe was used to monitor the block-skin contact temperature. Only the weight of the block was used to create the burns and no additional pressure was applied. (c) and (d) Representative hematoxylin and eosin stained histology images of (c) 10-s and (d) 40-s burns at 8 hpb. The asterisk points to an empty cavity of the pilosebaceous unit in the 10-s burn, and the arrowhead points to eosinophilic collagen fibers in the 40-s burn tissue. The thickness of the burn was determined to be corresponding to the deepest identified histologic feature within the burn wound as indicated by the vertical double arrows. The scale bars are 1 mm.

Fig. 1(b) shows a typical speckle contrast map (K^2 -map) of a flow phantom with significant static scattering as measured by the system. The embedded perfused region, outlined in dashed lines, is clearly observed. Figure 1(c) presents the results of K^2 and relative speckle correlation time, τ_c^{-1} , against actual flow speed, v , in a phantom with insignificant static scattering. Here, τ_c^{-1} was retrieved using Eq. (5) with $K_s = 0$. Note that K^2 versus v is plotted in a double-logarithmic scale and that error bars represent standard deviations. The linear relationship of K^2 and relative τ_c^{-1} with flow speed is evidently visible ($R^2 = 0.943$ for τ_c^{-1}). Despite K^2 values being extracted from H.264 video compressed data (possibly with reduced precision due to the lossy raw data compression), these results validate the camera-phone LASCA imaging prototype for accurate perfusion measurements when no or insignificant static scattering is present. Figure 1(d) depicts K^2 and relative τ_c^{-1} versus v in a phantom with significant static scattering prior to (open circles) and following (solid circles) correction of K^2 and τ_c^{-1} for static scattering. Note that K^2 versus v is plotted in a double-logarithmic scale and error bars are standard deviations. The SDR of this phantom, which quantifies the static-to-dynamic scattering composition ratio of the sample, was calculated using Eq. (3) to be 20-fold larger than that of the phantom with insignificant static scattering. The data clearly show that the linearity of K^2 and relative τ_c^{-1} measurements obtained by traditional LASCA (which does not correct for static scattering) breaks down in the presence of static scatterers ($R^2 = 0.414$ for τ_c^{-1}), whereas LASCA with correction of K^2 and τ_c^{-1} for static scattering [via $K^2 \rightarrow K^2 - K_s^2$ and Eq. (5), respectively] preserves the linearity of K^2 and relative τ_c^{-1} even when static scatterers are present ($R^2 = 0.946$ for τ_c^{-1}). Although speckle contrast data were computed from H.264 compressed videos (possibly with reduced precision compared to uncompressed video data), these results confirm the ability of the camera-phone LASCA imaging system with correction for static scattering, termed stLASCA as

previously noted, to provide corrected estimates for the relative static-to-dynamic scattering composition ratio and flow speed in samples consisting of both dynamic and static scatterers.

3.2 Camera-Phone Static Laser Speckle Contrast Analysis Imaging of Burn Phantoms

To explore the applicability of the camera-phone stLASCA prototype in burn diagnosis, burn phantoms of different depth and perfusion rate conditions were studied (see Sec. 2.3). Figure 3(a) shows the behavior of the normalized K^2 versus thickness of the simulated burn, Δz , at flow speeds of $v = 3$ mm/s (solid circles) and $v = 10$ mm/s (up-pointing triangles) in the phantoms. From Fig. 3(a), we can clearly see that K^2 increases with thickness of the simulated burn for both flow speeds, validating the known result that speckle contrast increases with burn severity.²⁹ However, K^2 increases differently for the two flow speeds as indicated by the gap between the solid and dashed lines in Fig. 3(a). In particular, while relative changes in flow speed were detectable by K^2 at simulated burn depths as low as $\Delta z = 0.3$ mm, no relative changes in flow speed were reliably measured by K^2 at larger depths. The increase in speckle contrast for the deeper burn phantoms should therefore be due to higher static scattering in these phantoms, rather than reduced perfusion as typically assumed for an increase in speckle contrast in the absence of static scatterers.^{1,21} These results reinforce the fact that interpretation of the spatial laser speckle contrast as an accurate estimate of relative flow speed can be confounded by the presence of static scattering.

To obtain improved information on the nonperfusion and perfusion components in the burn phantoms, we extracted from the measured speckle contrast, the SDR and τ_c^{-1} , for each phantom using Eqs. (3) and (5), respectively. Figures 3(b) and 3(c) depict the normalized SDR against thickness of the simulated burn, Δz , and a bar graph of the relative τ_c^{-1} values,

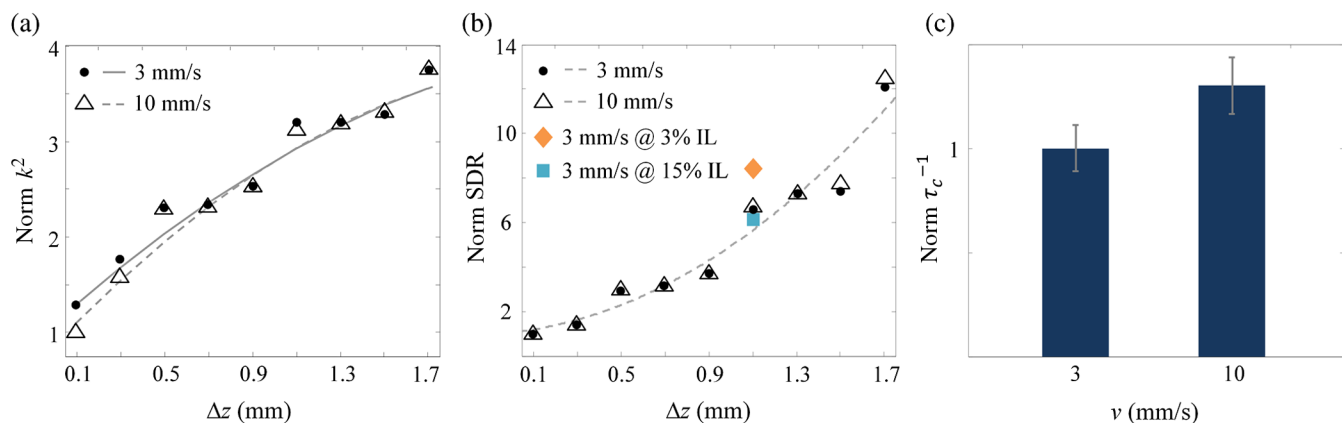


Fig. 3 Camera-phone static laser speckle contrast analysis imaging of burn phantoms. (a) Dependence of normalized K^2 on simulated burn layer depth, Δz , for perfusion rates of $v = 3$ mm/s (solid circles) and $v = 10$ mm/s (up-pointing triangles). K^2 was normalized to the lowest K^2 value obtained at $\Delta z = 0.1$ mm and $v = 10$ mm/s. Solid and dashed lines are drawn to guide the eyes for K^2 values measured at $v = 3$ and 10 mm/s, respectively. Repeated measurement standard deviations were negligible and are not presented for clarity. (b) Dependence of the normalized statically-to-dynamically scattered light ratio (SDR) of the burn phantoms on Δz for perfusion rates of $v = 3$ mm/s (solid circles) and $v = 10$ mm/s (up-pointing triangles). Normalized SDR values are also shown for Intralipid concentrations of 3% (orange diamond) and 15% (cyan square) at $\Delta z = 1.1$ mm and $v = 3$ mm/s. SDR values were normalized to the SDR obtained at $\Delta z = 0.1$ mm and $v = 10$ mm/s. Dashed line is drawn to guide the eyes. Repeated measurement standard deviations were negligible and are not presented for clarity. (c) Bar graph of normalized τ_c^{-1} values obtained from burn phantoms of $\Delta z = 0.1$ to 1.7 mm and $v = 3$ and 10 mm/s. Normalization of τ_c^{-1} was performed with respect to its average value at $v = 3$ mm/s.

respectively. Figure 3(b) clearly shows that the normalized SDR increases identically with the thickness of the simulated burn for the two flow speeds used in the experiments. Furthermore, reduction and increase of the Intralipid concentration in the 1.1-mm burn phantom raised and lowered the normalized SDR at $v = 3$ mm/s, respectively, as shown in Fig. 3(b), for Intralipid concentrations of 3% (orange diamond) and 15% (cyan square). Similar results were obtained at flow speed of $v = 10$ mm/s but are not shown for clarity of the plot. These findings suggest that the SDR of a burn wound can convey useful information on the static-to-dynamic scattering composition ratio of the burn regardless of blood perfusion irregularities in the wound, thereby providing a novel nonperfusion measure for discriminating burns of different severity. Finally, we note from Fig. 3(c) that the corrected estimator for relative τ_c^{-1} [Eq. (5)] can detect the difference between the two flow speeds used in the various burn phantoms with a p -value of 0.15.

3.3 Camera-Phone Static Laser Speckle Contrast Analysis Imaging of Porcine Burn Model *In Vivo*

We next tested the camera-phone stLASCA system for burn diagnosis *in vivo* using a porcine burn model (see Sec. 2.4). To determine the actual depth of the different burns, inflicted by a hot probe with contact times of 10, 20, 30, and 40 s, a histologic analysis was performed. Figures 2(c) and 2(d) show representative histology images of 10- and 40-s burns at 8 hpb, respectively. The histologic depth of the burns, indicated with a vertical double arrow, was determined to be corresponding to the deepest identified histologic feature from amongst several criteria (see Sec. 2.5). For example, the thickness of the 10-s burn in Fig. 2(c) was determined by the location of the empty cavity of the pilosebaceous unit (pointed by the asterisk), whereas the thickness of the 40-s burn in Fig. 2(d) was resolved by identifying eosinophilic collagen fibers in the tissue (pointed by the arrowhead). Figure 4 shows box plot representation of histologic burn depth by four burn groups (of contact times of 10, 20, 30, and 40 s) at 8, 32, and 104 hpb. These plots reveal that only the 10- and 40-s burns were statistically distinct over the entire course of the longitudinal study. This result may

stem from the limited burns thickness and relatively large variability of burn depth within each burn group obtained by the infliction technique used here. Burn wounds created with devices designed to apply a controlled, reproducible pressure to the animal skin could probably improve the statistical significance between burn groups of different contact time.²⁹ Nevertheless, statistically significant correlations between probe contact time and histologic burn depth were found over the entire course of the experiment ($r = 0.75, 0.7, 0.66$ at 8, 32, and 104 hpb, respectively; $n = 16$). Note that the progressive decrease in correlation over time may be due to the dynamic evolution of the burns.³⁰

To study the ability of the camera-phone stLASCA imaging instrument to distinguish burns of different depths (and hence severity), we measured the speckle contrast for the different burns at 8, 32, and 104 hpb. Figure 5 presents representative color photos of 10- and 40-s burns at 2 hpb along with the corresponding normalized K^2 -maps measured at 8, 32, and 104 hpb. While the image of the 10-s burn showed white and pink areas at the wound site, the photo of the 40-s burn appeared white throughout the entire wound region, allowing one to visually distinguish 10-s burns from 40-s burns. Inspection of the corresponding normalized K^2 -maps reveals that of the 10- and 40-s burns experienced a different increase in speckle contrast over the course of the study relative to normal skin. Specifically, while a similar increase in speckle contrast was found for both types of burns at 8 hpb, the more severe 40-s burns exhibited a slower recovery of the speckle contrast over time as can be observed from Fig. 5. We note that in contrast to the 10- and 40-s burns, the 20- and 30-s burns were indistinguishable by eye from the 40-s burns at 2 hpb [see Fig. 2(a)], and their corresponding normalized K^2 maps appeared relatively similar to that of the 40-s burns at 8 and 32 hpb (data not shown).

To quantify relative changes in the speckle contrast images of the porcine burns with respect to normal porcine skin, we generated the box plot of relative K^2 by the four burn groups (of contact times of 10, 20, 30, and 40 s) at 8, 32, and 104 hpb, as presented in Fig. 6(a). The figure shows a considerable increase in K^2 at 8 hpb relative to normal skin for all burn types. However, no significant difference between the four burn groups

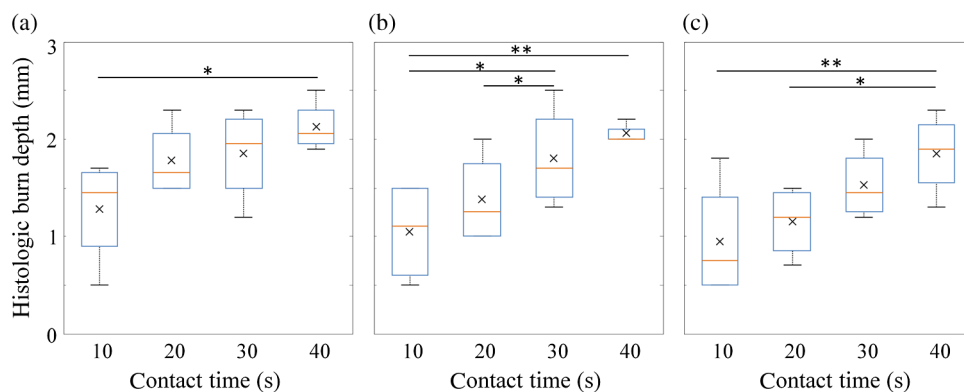


Fig. 4 Box and whisker plots of histologic burn depth for four porcine burn groups of different contact times of 10, 20, 30, and 40 s. Plots are shown for (a) 8 hpb, (b) 32 hpb, and (c) 104 hpb. The boxes represent the median (orange middle line) and mean (black cross) limited by the 25th (Q1) and 75th (Q3) percentiles. The whiskers are the upper and lower adjacent values, which are the most extreme values within $Q3 + 1.5(Q3 - Q1)$ and $Q1 - 1.5(Q3 - Q1)$, respectively. Single and double asterisks represent statistically significant differences between burn groups ($P < 0.05$ and $P < 0.01$, respectively). The number of biopsied burns obtained at each contact time was 4.

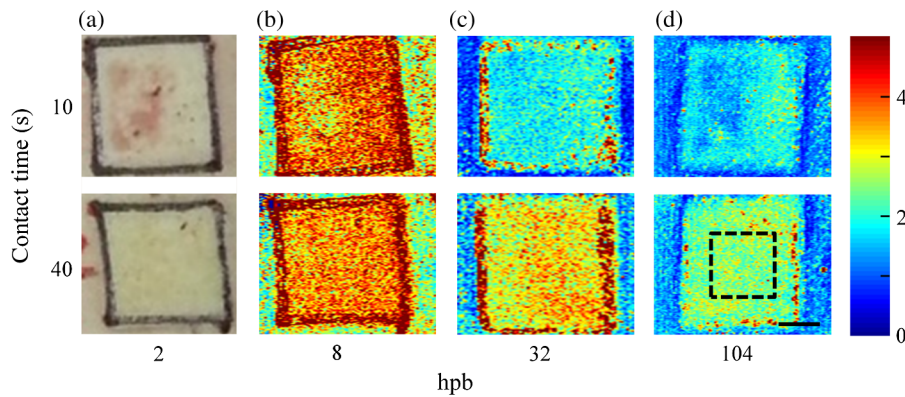


Fig. 5 Representative color photos of 10-s and 40-s porcine burns at (a) 2 hpb alongside with the corresponding normalized K^2 -maps at (b) 8 hpb, (c) 32 hpb, and (d) 104 hpb (top row: 10-s burns, bottom row: 40-s burns). Normalization of K^2 was performed with respect to K^2 of normal porcine skin. High and low normalized K^2 levels are indicated in red and blue colors, respectively. The outlined region represents the central burn area. The scale bar is 10 mm.

was detected by K^2 at 8 hpb, possibly due to the limited graded burn severity obtained by the infliction probe and the complex pathophysiology of thermal burns a few hours following injury. At 32 hpb, K^2 of the different burn groups remained higher than that of normal skin; yet, normalized K^2 median values were lower than those recorded at 8 hpb, pointing on a possible initial recovery of the burns. In addition, normalized K^2 measured at 32 hpb showed a statistically significant correlation to infliction contact times ($r = 0.84$, $n = 29$) and significantly distinguished the 40-s burns from the three other burn types, and the 30-s

burns from the 10-s burns. At 104 hpb, K^2 was still higher than that of normal skin for all burn types and its median values were lower than those estimated at 32 hpb, implying the progress of healing of the wounds. Furthermore, normalized K^2 at 104 hpb presented a statistically significant correlation to probe contact times ($r = 0.77$, $n = 14$) but could significantly distinguish between the 40- and 10-s burns only.

We further extracted from the measured speckle contrast improved information on the nonperfusion and perfusion components in the porcine burns by computing the SDR and τ_c^{-1} for

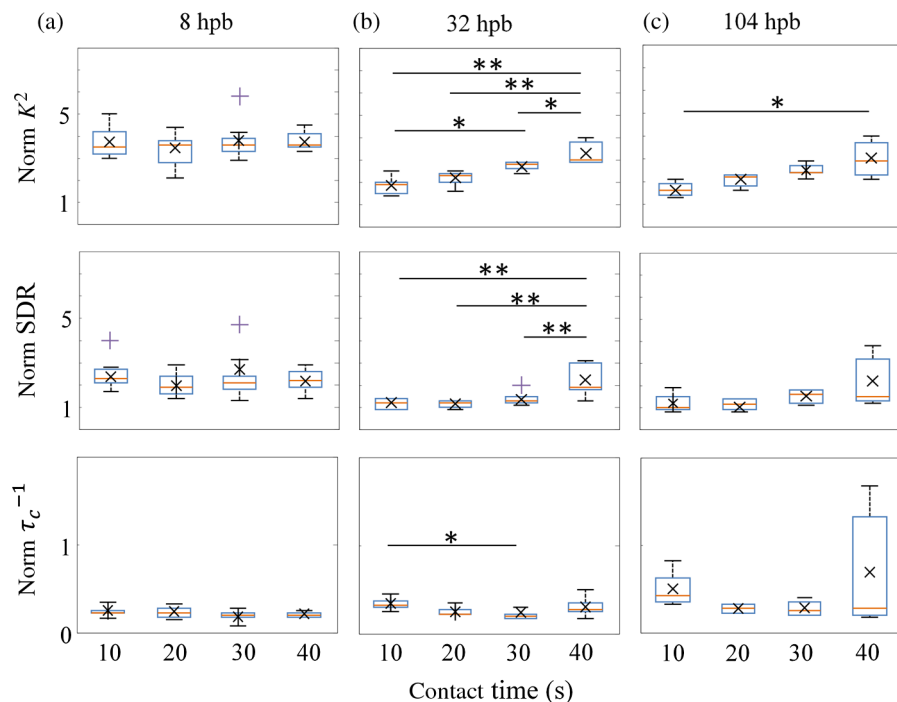


Fig. 6 Box and whisker plots of normalized (a) K^2 , (b) SDR, and (c) τ_c^{-1} for four porcine burn groups of different contact times of 10, 20, 30, and 40 s. Plots are shown for 8, 32, and 104 hpb. K^2 , SDR, and τ_c^{-1} were normalized to K^2 , SDR, and τ_c^{-1} of normal porcine skin. The boxes and whiskers signify the same as in Fig. 4. The purple plus signs represent outliers. Single and double asterisks denote statistically significant differences between burn groups ($P < 0.05$ and $P < 0.01$, respectively). The number of burns used in the statistical analysis was as follows: at 8 hpb, 43 burns (11 burns at each of the contact times of 10, 20, 30 s and 10 burns at 40-s contact time); at 32 hpb, 29 burns (8 burns at 10-s contact time and 7 burns at each of the contact times of 20, 30, and 40 s); and at 104 hpb, 14 burns (4 burns at each of the contact times of 10 and 20 s, and 3 burns at each of the contact times of 30 and 40 s).

each burn [using Eqs. (3) and (5), respectively], and subsequently quantifying their change relative to the SDR and τ_c^{-1} of normal porcine skin, respectively. Figures 6(b) and 6(c) show, respectively, the box plots of relative SDR and τ_c^{-1} by the four burn groups (of contact times of 10, 20, 30, 40 s) at 8, 32, and 104 hpb. A few points can be drawn from these figures as follows: (i) At 8 hpb, all burn types experienced an increase in SDR and a decrease in τ_c^{-1} relative to normal skin, implying the higher static-to-dynamic scattering composition ratio and lower blood perfusion of the wounds (with respect to normal porcine skin). However, similarly to the speckle contrast measured at 8 hpb [Fig. 6(a)], no significant difference between the four burn groups was identified neither by the SDR nor by τ_c^{-1} at 8 hpb. (ii) At 32 hpb, the median values of the normalized SDR (τ_c^{-1}) of the four burn groups remained higher (lower) than those measured for normal skin but lower (higher) than those at 8 hpb, indicating a possible initial recovery of the burns. Most importantly, while SDR at 32 hpb showed a statistically significant correlation to probe contact times ($r = 0.67$, $n = 29$) and significantly distinguished the 40-s burns from the three other burn types, τ_c^{-1} at 32 hpb presented a statistically insignificant correlation to infliction contact times and significantly distinguished between the 30- and 10-s burns only. These results show that the SDR, rather than τ_c^{-1} , can largely control the ability of the measured speckle contrast to distinguish burns of different severity with statistical significance, suggesting that relative changes in the static-to-dynamic scattering composition of burns can dominate relative changes in blood flow for burns of different depth. (iii) At 104 hpb, the median SDR (τ_c^{-1}) of the four burn groups remained higher (lower) than that measured for normal skin but was lower (higher) than those at 32 hpb (except for the SDR of the 30-s burns), implying the progress of healing of the burns in terms of reduced static-to-dynamic scattering composition ratio and increased blood perfusion of the wounds. Unlike speckle contrast measured at 104 hpb, no significant difference between the four burn groups was identified neither by the SDR nor by τ_c^{-1} [probably due to the noisier estimates for SDR and τ_c^{-1} at 104 hpb, as seen in Figs. 6(b) and 6(c), respectively].

Comparison of our speckle contrast results for the graded porcine burns with those obtained recently by Ponticorvo et al.⁸ using spatial LSI with a scientific-grade monochrome camera^{29,31} reveals that, in both studies, all porcine burns experienced an increase in K^2 relative to that of normal skin and shows that K^2 had an increasing trend with burn severity at times longer than 8 hpb [see Fig. 6(a) here and Fig. 5(b) in Ref. 29]. Note that K^2 is proportional to the reciprocal of the speckle flow index,³¹ used in Ref. 29. Although this similarity is not unexpected (as both spatial LSI and stLASCA use spatial sampling of speckle to measure the speckle contrast), stLASCA introduces a previously neglected correction of speckle contrast for static scattering in burn wounds, providing corrected estimates and improved interpretation of nonperfusion and perfusion information on the wounds in terms of the static-to-dynamic scattering composition ratio and blood perfusion, respectively [see Figs. 6(b) and 6(c)]. Note that the difference between the speckle contrast results here and in Ref. 29 at times ≤ 8 hpb may be associated to different porcine models and burn infliction techniques used.

4 Conclusions

We have demonstrated a noninvasive and contactless camera-phone stLASCA imaging system for assessing burn severity

in an animal model *in vivo*. The system incorporated an improved processing scheme with a previously neglected correction of speckle contrast against statically scattered light from the burn wound. This processing scheme was shown to provide corrected estimation for the perfusion and nonperfusion components in the burn by means of the reciprocal of the speckle correlation time (τ_c^{-1}) and the SDR, respectively, thereby facilitating interpretation of speckle contrast data of burn wounds. In particular, using stLASCA of graded porcine burns, we showed that the SDR (which measures the static-to-dynamic scattering composition ratio of the wound), rather than τ_c^{-1} (which is proportional to the blood perfusion rate in the burn), can largely control the ability of the measured speckle contrast to distinguish burns of different severity with statistical significance during the first 48 hpb, suggesting that relative changes in the static-to-dynamic scattering composition of burns can dominate those in blood flow for burn wounds of different severity.

Although the current system employed a large red illumination laser and a zoom magnifying lens, compact laser diode modules and detachable camera-phone zoom lenses could be used in the future.^{16,17} In addition, camera-phone stLASCA devices could enable imaging of bigger burn surfaces by utilizing wider illumination and larger image sensors and could be designed to be handheld using numerical image stabilization methods, such as speckle image registration.³² Finally, we envision that speckle contrast maps, SDR, and τ_c^{-1} values could ultimately be generated by a smartphone application within several tens of milliseconds.¹⁴

Appendix

This appendix describes the model for the squared spatial laser speckle contrast, K^2 , and follows the formalism described by Zakharov et al.^{9,10} Consider a coherent light source illuminating a scattering medium with static and dynamic scatterers. Light waves propagate in the medium and are backscattered off both types of scatterers, forming speckle intensity patterns that are detected by the camera sensor. An expression for the squared spatial contrast of the time-integrated speckle intensity pattern can be derived to be^{1,9,10}

$$K^2 = \frac{2\beta}{T} \int_0^T \left(1 - \frac{\tau}{T}\right) |g_1(\tau)|^2 d\tau, \quad (6)$$

where β is a normalization coefficient (so-called coherence factor), T is the camera integration time, and $g_1(\tau)$ represents the normalized temporal correlation function of the static and dynamic electric fields and is given by^{9,10,33}

$$g_1(\tau) = (1 - \rho) |g_d(\tau)| + \rho, \quad (7)$$

where $g_d(\tau)$ is the normalized temporal correlation function of the dynamic electric field (with characteristic decay time of τ_c) and ρ is the fraction of total light intensity that is statically back-scattered and reads as

$$\rho = \frac{I_s}{I_s + I_d}, \quad (8)$$

where I_s and I_d are the mean intensities of light scattered from the static and dynamic scatterers in the imaged medium, respectively. By substituting Eq. (7) into Eq. (6), K^2 can be written as

$$K^2 = (1 - \rho)^2 \frac{2\beta}{T} \int_0^T \left(1 - \frac{\tau}{T}\right) |g_d(\tau)|^2 d\tau + 2\rho(1 - \rho) \frac{2\beta}{T} \int_0^T \left(1 - \frac{\tau}{T}\right) |g_d(\tau)| d\tau + \beta\rho^2, \quad (9)$$

where the first two terms on the right hand side of Eq. (9) comprise the dynamic (perfusion) part of the squared speckle contrast, K_d^2 , and the third term represents the static (nonperfusion) component of K^2 , denoted by K_s^2 . To evaluate K_s^2 , assume that the camera frame rate T_0^{-1} satisfies $T_0 \gg \tau_c$, and thus the spatial cross-correlation of two time-sequential speckle frames at zero spatial shift essentially includes only the static speckle component.^{9,10,34} Using the Siegert relation,³⁴ K_s^2 can now be expressed as

$$K_s^2 = g_2(T_0) - 1 = \frac{\langle I(t)I(t+T_0) \rangle}{\langle I(t) \rangle \langle I(t+T_0) \rangle} - 1, \quad (10)$$

with $g_2(\tau)$ representing the normalized temporal intensity auto-correlation function, $I(t)$ being the speckle intensity recorded at time t , and $\langle \rangle$ denoting spatial (or ensemble) averaging over an observation window in space. Next, by substituting the value of K_s from Eq. (10) into Eq. (3) and calibrating β using a Teflon slab,^{9,10} the SDR of turbid media can be estimated.

Finally, to effectively assess the reciprocal of the speckle correlation time, τ_c^{-1} , in scattering media, assume the following normalized correlation functions $g_d(\tau) = e^{-|\tau|/\tau_c}$ or $g_d(\tau) = e^{-\sqrt{\tau/\tau_c}}$ for samples with backscattering ballistic and diffusive dynamics,^{9-12,34} respectively. Using the above models for $g_d(\tau)$ in Eq. (9) with $T \gg \tau_c$, τ_c^{-1} can readily be derived as Eq. (5).

Acknowledgments

This work was financially supported by the Israel Ministry of Economy through the Kamin program. I. R. gratefully acknowledges the support of the Azrieli Foundation under the Israeli graduate studies fellowship program.

References

1. D. A. Boas and A. K. Dunn, "Laser speckle contrast imaging in biomedical optics," *J. Biomed. Opt.* **15**(1), 011109 (2010).
2. A. F. Fercher and J. D. Briers, "Flow visualization by means of single-exposure speckle photography," *Opt. Commun.* **37**(5), 326–330 (1981).
3. H. Cheng and T. Q. Duong, "Simplified laser-speckle-imaging analysis method and its application to retinal blood flow imaging," *Opt. Lett.* **32**(15), 2188–2190 (2007).
4. H. Cheng, Y. Yan, and T. Q. Duong, "Temporal statistical analysis of laser speckle images and its application to retinal blood-flow imaging," *Opt. Express* **16**(14), 10214–10219 (2008).
5. A. K. Dunn et al., "Dynamic imaging of cerebral blood flow using laser speckle," *J. Cereb. Blood Flow Metab.* **21**(3), 195–201 (2001).
6. T. Durdurán et al., "Spatiotemporal quantification of cerebral blood flow during functional activation in rat somatosensory cortex using laser-speckle flowmetry," *J. Cereb. Blood Flow Metab.* **24**(5), 518–525 (2004).
7. N. Hecht et al., "Laser speckle imaging allows real-time intraoperative blood flow assessment during neurosurgical procedures," *J. Cereb. Blood Flow Metab.* **33**(7), 1000–1007 (2013).

8. B. Choi, N. M. Kang, and J. S. Nelson, "Laser speckle imaging for monitoring blood flow dynamics in the in vivo rodent dorsal skin fold model," *Microvasc. Res.* **68**(2), 143–146 (2004).
9. P. Zakharov et al., "Quantitative modeling of laser speckle imaging," *Opt. Lett.* **31**(23), 3465–3467 (2006).
10. P. Zakharov et al., "Dynamic laser speckle imaging of cerebral blood flow," *Opt. Express* **17**(16), 13904–13917 (2009).
11. A. B. Parthasarathy et al., "Robust flow measurement with multi-exposure speckle imaging," *Opt. Express* **16**(3), 1975–1989 (2008).
12. A. B. Parthasarathy, S. M. Kazmi, and A. K. Dunn, "Quantitative imaging of ischemic stroke through thinned skull in mice with multi exposure speckle imaging," *Biomed. Opt. Express* **1**(1), 246–259 (2010).
13. D. Zölei et al., "Multiple exposure time based laser speckle contrast analysis: demonstration of applicability in skin perfusion measurements," *Photonics Optoelectron.* **1**(2), 28–32 (2012).
14. I. Remer and A. Bilencia, "Laser speckle spatiotemporal variance analysis for noninvasive widefield measurements of blood pulsation and pulse rate on a camera-phone," *J. Biophotonics* (2015).
15. O. Yang and B. Choi, "Laser speckle imaging using a consumer-grade color camera," *Opt. Lett.* **37**(19), 3957–3959 (2012).
16. L. M. Richards et al., "Low-cost laser speckle contrast imaging of blood flow using a webcam," *Biomed. Opt. Express* **4**(10), 2269–2283 (2013).
17. D. Jakovels et al., "Mobile phone based laser speckle contrast imager for assessment of skin blood flow," *Proc. SPIE* **9421**, 94210J (2014).
18. Laser Institute of America, *American National Standard for Safe Use of Lasers*, ANSI Z136.1–2007, American National Standards Institute, New York (2007).
19. http://www.gsmarena.com/sony_ericsson_xperia_arc-3619.php
20. I. E. Richardson, *The H.264 Advanced Video Compression Standard*, pp. 81–91, Wiley, Chichester (2010).
21. J. D. Briers, G. Richards, and X. W. He, "Capillary blood flow monitoring using laser speckle contrast analysis (LASCA)," *J. Biomed. Opt.* **4**(1), 164–175 (1999).
22. J. C. Ramirez-San-Juan et al., "Impact of velocity distribution assumption on simplified laser speckle imaging equation," *Opt. Express* **16**(5), 3197–3203 (2008).
23. A. Sathwani et al., "Determination of teflon thickness with laser speckle. I. Potential for burn depth diagnosis," *Appl. Opt.* **35**(28), 5727–5735 (1996).
24. L. Wang and S. L. Jacques, "Use of a laser beam with an oblique angle of incidence to measure the reduced scattering coefficient of a turbid medium," *Appl. Opt.* **34**(13), 2362–2366 (1995).
25. X. Wang and R. M. Kimble, "A review on porcine burn and scar models and their relevance to humans," *Wound Pract. Res.* **18**(1), 41–49 (2010).
26. A. Papp et al., "The progression of burn depth in experimental burns: a histological and methodological study," *Burns* **30**(7), 684–690 (2004).
27. T. W. Panke and C. G. McLeod, *Pathology of Thermal Injury: A Practical Approach*, Grune & Stratton, Florida (1985).
28. K. M. Cross, "Assessment of tissue viability in acute thermal injuries using near infrared point spectroscopy," PhD Thesis, Univ. of Toronto (2010).
29. A. Ponticorvo et al., "Quantitative assessment of graded burn wounds in a porcine model using spatial frequency domain imaging (SFDI) and laser speckle imaging (LSI)," *Biomed. Opt. Express* **5**(10), 3467–3481 (2014).
30. A. D. Jaskille et al., "Critical review of burn depth assessment techniques: Part I. Historical review," *J. Burn Care Res.* **30**(6), 937–947.
31. O. Yang, D. Cuccia, and B. Choi, "Real-time blood flow visualization using the graphics processing unit," *J. Biomed. Opt.* **16**(1), 016009 (2011).
32. P. Miao et al., "High resolution cerebral blood flow imaging by registered laser speckle contrast analysis," *IEEE Trans. Biomed. Eng.* **57**, 1152–1157 (2010).
33. D. A. Boas and A. G. Yodh, "Spatially varying dynamical properties of turbid media probed with diffusing temporal light correlation," *J. Opt. Soc. Am. A* **14**(1), 192–215 (1997).
34. R. Bandyopadhyay et al., "Speckle-visibility spectroscopy: a tool to study time-varying dynamics," *Rev. Sci. Instrum.* **76**, 093110 (2005).